JACS
JOURNAL OF THE AMERICAN CHEMICAL SOCIETY
Article
pubs.acs.org/JACS

Origin of the High Performance in GeTe-Based Thermoelectric Materials upon Bi_2Te_3 Doping

Di Wu,[†,#] Li-Dong Zhao,[‡,#] Shiqiang Hao,[§] Qike Jiang,[†] Fengshan Zheng,[†] Jeff W. Doak,[§] Haijun Wu,[†] Hang Chi,[∥] Y. Gelbstein,[⊥] C. Uher,[∥] C. Wolverton,[§] Mercouri Kanatzidis,*[,‡] and Jiaqing He*[,†]

[†]Department of Physics, South University of Science and Technology of China, Shenzhen 518055, P. R. China
[‡]Department of Chemistry, Northwestern University, Evanston, Illinois 60208, United States
[§]Department of Materials Science and Engineering, Northwestern University, Evanston, Illinois 60208, United States
[∥]Department of Physics, University of Michigan, Ann Arbor, Michigan 48109, United States
[⊥]Department of Materials Engineering, Ben-Gurion University of the Negev, Beer-Sheva 84105, Israel

Supporting Information

ABSTRACT: As a lead-free material, GeTe has drawn growing attention in thermoelectrics, and a figure of merit (ZT) close to unity was previously obtained via traditional doping/alloying, largely through hole carrier concentration tuning. In this report, we show that a remarkably high ZT of ~1.9 can be achieved at 773 K in $Ge_{0.87}Pb_{0.13}Te$ upon the introduction of 3 mol % Bi_2Te_3. Bismuth telluride promotes the solubility of PbTe in the GeTe matrix, thus leading to a significantly reduced thermal conductivity. At the same time, it enhances the thermopower by activating a much higher fraction of charge transport from the highly degenerate Σ valence band, as evidenced by density functional theory calculations. These mechanisms are incorporated and discussed in a three-band (L + Σ + C) model and are found to explain the experimental results well. Analysis of the detailed microstructure (including rhombohedral twin structures) in $Ge_{0.87}Pb_{0.13}Te$ + 3 mol % Bi_2Te_3 was carried out using transmission electron microscopy and crystallographic group theory. The complex microstructure explains the reduced lattice thermal conductivity and electrical conductivity as well.

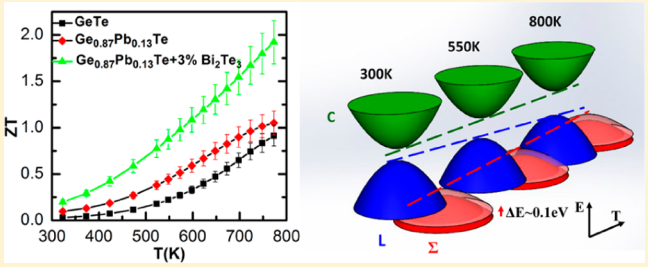

INTRODUCTION

The performance of a thermoelectric material is evaluated by a dimensionless figure of merit, $ZT = (S^2\sigma/\kappa)T$, where S, σ, κ, and T are the Seebeck coefficient (or thermopower), electrical conductivity, thermal conductivity, and absolute temperature, respectively. Improvements in the power factor $S^2\sigma$ can be achieved by tailoring the band structure,[1−3] while ultralow total thermal conductivity ($\kappa_{tot} = \kappa_{latt} + \kappa_{elec}$) can be realized through all-scale hierarchical architectures[4] and/or intrinsic bond anharmonicity.[5] Alloying/doping is widely utilized to optimize the electrical transport properties, control the solid solution behavior, and introduce precipitates and defects.[6,7]

Among the rapidly growing class of thermoelectric materials, the narrow-band-gap IV−VI compound GeTe has not attracted as much attention as other systems, but it is certainly of interest both from a scientific perspective and for potential applications in the medium-temperature range (600−900 K). GeTe is a heavily p-type semiconductor that exhibits a very high carrier concentration (~10^{21} cm^{-3})[8−11] because of a large number of Ge vacancies in its crystal structure.[12,13] GeTe undergoes a second-order ferroelectric transition from the cubic (β, high-temperature) phase to the rhombohedral (α, low-temperature) phase,[14,15] accompanied by an angular distortion of the unit cell from 60° to about 57.51° and a small ferroelectric displacement of the Ge sublattice along the [111] direction. The transition in GeTe occurs at $T_c \approx 700$ K but depends on alloying with other phases and doping levels.[16,17] Good thermoelectric properties were obtained at high temperature by doping/alloying GeTe with $AgSbTe_2$,[18] $AgBiTe_2$,[16] and Sb_2Te_3.[19] Christakudi et al.[8] systematically investigated the thermoelectric properties of GeTe alloys with varying Bi_2Te_3 content and interpreted their temperature and composition dependences in terms of the electronic band structures. Recently, we[20−22] also discovered that GeTe-based materials exhibit very high thermoelectric performance, but the underlying mechanism of the impressive properties remains unclear.

In this work, we studied the remarkable thermoelectric performance of Bi_2Te_3-doped $Ge_{0.87}Pb_{0.13}Te$ in terms of the influence of microstructures and electronic band structures. Pb was intended to suppress Ge vacancies, but above a certain limit (~5% at room temperature), Pb-rich phases precipitated and thus reduced the thermal conductivity. Bi_2Te_3 was introduced as a donor dopant to reduce the very high hole carrier concentration. However, we found that Bi_2Te_3 not only fulfills the role of a donor dopant but also serves two additional

Received: May 16, 2014
Published: July 29, 2014

   dx.doi.org/10.1021/ja504896a | J. Am. Chem. Soc. 2014, 136, 11412−11419

functions: (i) it reduces the thermal conductivity by enhancing point-defect scattering as it promotes the PbTe solubility in GeTe, and (ii) it enhances the thermopower through a modification of the relative energy of the light and heavy valence bands (L and Σ). That is, as suggested by both density functional theory (DFT) calculations and a three-band (L + Σ + C) model, the two bands get closer in energy when Bi_2Te_3 is added. Thus, it is possible to perform band engineering in the GeTe system using Bi_2Te_3 as an additive. Collectively, we show here that it is the beneficial integration of the power factor enhancement and the thermal conductivity reduction that leads to a ZT of ∼1.9 at 773 K in $Ge_{0.87}Pb_{0.13}Te$ + 3% Bi_2Te_3.

RESULTS AND DISCUSSION

Thermoelectric Transport Properties. Experimental procedures and calculation methods are detailed in the Supporting Information (SI). The rhombohedral phase of GeTe at room temperature was confirmed by powder X-ray diffraction (XRD) patterns, as shown in Figure 1a. GeTe was

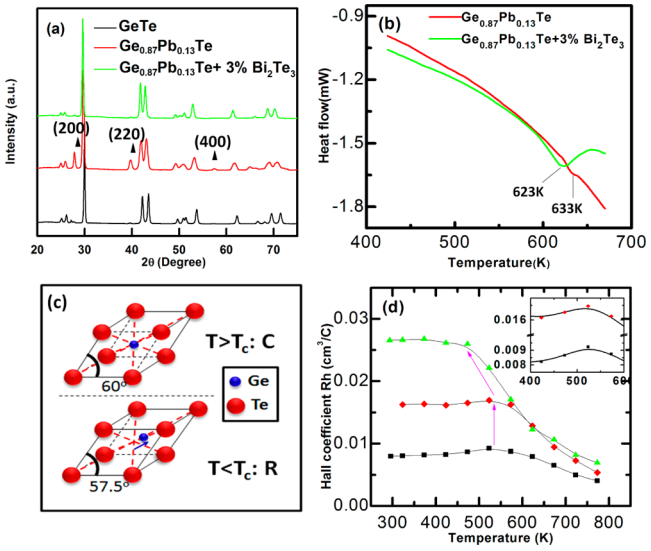

Figure 1. (a) Powder XRD patterns of GeTe, $Ge_{0.87}Pb_{0.13}Te$, and $Ge_{0.87}Pb_{0.13}Te$ + 3 mol % Bi_2Te_3. The black triangles mark the peaks of the face-centered cubic PbTe phase. (b) DSC curves for $Ge_{0.87}Pb_{0.13}Te$ and $Ge_{0.87}Pb_{0.13}Te$ + 3 mol % Bi_2Te_3 as labeled. (c) Schematic crystal structure for the cubic-to-rhombohedral phase transition. (d) Hall coefficients of GeTe, $Ge_{0.87}Pb_{0.13}Te$, and $Ge_{0.87}Pb_{0.13}Te$ + 3 mol % Bi_2Te_3 as functions of temperature. The inset shows the slight bumps between 400 and 600 K in the curves for GeTe and $Ge_{0.87}Pb_{0.13}Te$.

indexed to be solely rhombohedral, while peaks of cubic PbTe were found in the diffraction pattern of $Ge_{0.87}Pb_{0.13}Te$, indicating limited solubility of PbTe in the GeTe matrix. The immiscible PbTe content in the GeTe matrix was estimated to be ∼8% via XRD peaks, thus suggesting a solubility limit of ∼5% for PbTe at room temperature. This is in general agreement with the previously reported values of ≲5% by Volykhov et al.[23] and ≲4% by Mazelsky et al.[24] Nevertheless, when 3 mol % Bi_2Te_3 is doped into $Ge_{0.87}Pb_{0.13}Te$, the cubic PbTe phase nearly vanishes from the diffraction patterns, which indicates a remarkable enhancement of the solubility of PbTe in GeTe. This process in which a third agent (Bi_2Te_3) modulates the solubility of a second agent (PbTe) in GeTe is a surprising observation and has dramatic implications for the carrier concentration and the thermal conductivity of the material and, ultimately, for the thermoelectric performance.

The crystal structure evolution from the high-temperature ($T > T_c$) cubic phase to the low-temperature ($T < T_c$) rhombohedral phase in GeTe is schematically illustrated in Figure 1c. Differential scanning calorimetry (DSC) curves (Figure 1b) indicate that the phase transition temperatures in $Ge_{0.87}Pb_{0.13}Te$ and $Ge_{0.87}Pb_{0.13}Te$ + 3% Bi_2Te_3 are around 633 and 623 K, respectively, both of which are lower than that in pure GeTe ($T_c \approx 700$ K). The Hall carrier concentrations at room temperature derived from the data shown in Figure 1d are $(7.85 \pm 0.39) \times 10^{20}$ cm^{-3} for GeTe, $(3.85 \pm 0.19) \times 10^{20}$ cm^{-3} for $Ge_{0.87}Pb_{0.13}Te$, and $(2.34 \pm 0.12) \times 10^{20}$ cm^{-3} for $Ge_{0.87}Pb_{0.13}Te$ + 3 mol % Bi_2Te_3. The introduction of PbTe into the GeTe matrix leads to an over 50% reduction in the carrier concentration, while the addition of 3 mol % Bi_2Te_3 causes an additional 40% decrease. The former occurs because Pb fills the hole-generating Ge vacancies during PbTe dissolution,[25] thereby reducing the concentration of holes. The latter is ascribed to the enhanced dissolution of Ge atoms back into the Ge vacancies as a second phase associated with the presence of Bi_2Te_3.[12,25] This reduction in the carrier concentration of holes increases the thermopower in $Ge_{0.87}Pb_{0.13}Te$ + 3 mol % Bi_2Te_3 relative to those of GeTe and $Ge_{0.87}Pb_{0.13}Te$. The hole concentrations stay almost constant over the temperature range 300−450 K. The inset of Figure 1d shows slight bumps in the temperature dependence of the Hall coefficient (R_H) between 450 and 600 K for GeTe and $Ge_{0.87}Pb_{0.13}Te$, attributed to the convergence of the two valence bands (L and Σ) (also discussed below). At temperatures above ∼550 K for $Ge_{0.87}Pb_{0.13}Te$ and above ∼500 K for $Ge_{0.87}Pb_{0.13}Te$ + 3 mol % Bi_2Te_3, R_H decreases rapidly, and the single-carrier band transport assumed in the analysis of the Hall effect no longer applies because contributions of the second valence band (due to intrinsic excitation of electrons from Σ to L) become significant.[26] The decreasing tendency of R_H is not related to the phase transition because the transition temperatures are ∼633 and ∼623 K for $Ge_{0.87}Pb_{0.13}Te$ and $Ge_{0.87}Pb_{0.13}Te$ + 3 mol % Bi_2Te_3, respectively, as evidenced from the DSC measurements (Figure 1b).

The temperature dependence of thermoelectric properties of GeTe, $Ge_{0.87}Pb_{0.13}Te$, and $Ge_{0.87}Pb_{0.13}Te$ + 3 mol % Bi_2Te_3 is shown in Figure 2. The thermopowers of GeTe and $Ge_{0.87}Pb_{0.13}Te$ show a steadily increasing trend with temperature, while the thermopower of $Ge_{0.87}Pb_{0.13}Te$ + 3 mol % Bi_2Te_3 climbs much more rapidly in the low and intermediate temperature range. The latter reaches a maximum of 273 μV/K at 773 K, while the values for GeTe and $Ge_{0.87}Pb_{0.13}Te$ are only 167 and 180 μV/K, respectively, at the same temperature (Figure 2a). Below we will show that the significantly enhanced thermopower can be attributed to a combination of the reduced carrier concentration and the augmented heavy valence band contribution. The electrical conductivities (σ) of all three compositions decrease with elevating temperature (Figure 2b), indicating their metallic transport characters. At 323 K, σ drops dramatically from ∼7698 S/cm for GeTe to ∼3323 S/cm for $Ge_{0.87}Pb_{0.13}Te$ and to 1529 S/cm for $Ge_{0.87}Pb_{0.13}Te$ + 3 mol % Bi_2Te_3, which is consistent with the decreasing carrier concentration (Figure 1d). This confirms that Pb alloying and Bi doping indeed suppress the Ge vacancies. The solid lines shown in Figure 2a,b are the calculations based on a three-band Kane model, which is discussed below and also in the

dx.doi.org/10.1021/ja504896a | J. Am. Chem. Soc. 2014, 136, 11412−11419

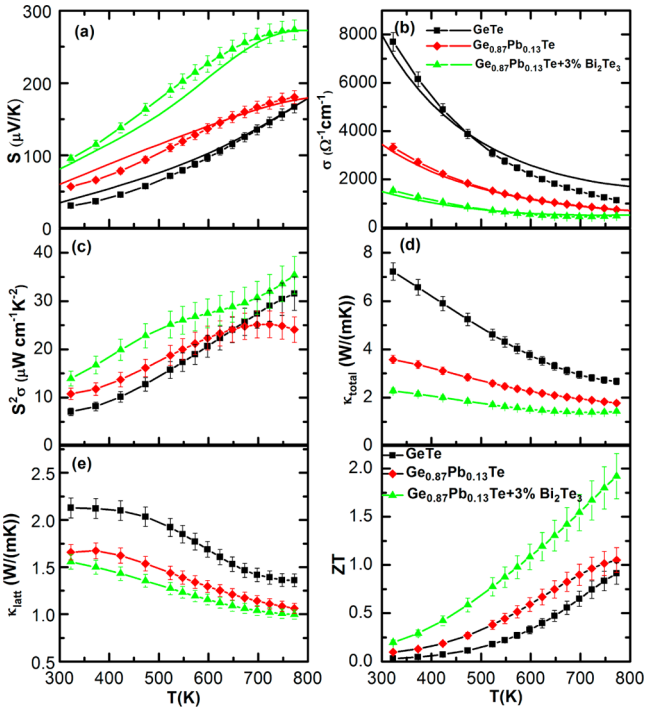

Figure 2. Calculated (solid lines) and experimental (line+symbols) (a) thermopower S, (b) electrical conductivity σ, (c) Power Factor $S^2\sigma$, (d) total thermal conductivity κ_{total}, (e) lattice thermal conductivity κ_{latt} and (f) figure of merit ZT of GeTe (black), $Ge_{0.87}Pb_{0.13}Te$ (red) and $Ge_{0.87}Pb_{0.13}Te$ + 3 mol % Bi_2Te_3 (green), respectively.

Supporting Information. At 773 K, the highest power factor ($S^2\sigma$) of 35 μW cm^{-1} K^{-2} is exhibited by the 3 mol % Bi_2Te_3 doped $Ge_{0.87}Pb_{0.13}Te$ (Figure 2c), in contrast to ~30 μW cm^{-1} K^{-2} for GeTe and ~25 μW cm^{-1} K^{-2} for $Ge_{0.87}Pb_{0.13}Te$.

The total thermal conductivity (κ_{tot}) (Figure 2d) shows a notable reduction upon the introduction of PbTe and Bi_2Te_3, especially in the low-temperature region. κ_{tot} is the sum of the electronic (κ_{elec}) and lattice (κ_{latt}) thermal conductivities. κ_{elec} is proportional to the electrical conductivity (σ) through the Wiedemann–Franz relation, $\kappa_{elec} = L\sigma T$, where the Lorenz number L is normally derived by fitting the respective thermopower values (in a single band assumption) as described elsewhere.[27] In this work, it was recalculated within the three-band model, where two-carrier transport (light and heavy holes) and bipolar diffusion are explicitly included. The temperature-dependent Lorenz number is given in Figure S1a in the Supporting Information, and κ_{latt} (Figure 2e) was obtained by direct subtraction of κ_{elec} (Figure S1b) from κ_{tot}. The lattice thermal conductivities have similar decreasing trends for all three compositions. Moreover, κ_{latt} is reduced by ~22% upon Pb alloying and further reduced by an additional ~5% after Bi_2Te_3 doping as observed over the entire measured temperature range. As a result of the enhanced power factor $S^2\sigma$ and reduced thermal conductivity κ_{tot}, ZT reaches the highest value of ~1.9 at 773 K for $Ge_{0.87}Pb_{0.13}Te$ + 3 mol % Bi_2Te_3, in contrast to only ~0.9 for GeTe and ~1.1 for $Ge_{0.87}Pb_{0.13}Te$ (Figure 2f).

The understanding of the effects of the microstructures and the behavior of the band structure will be discussed in the following sections. More detailed microstructure analysis and transport property calculations can be found in the Supporting Information.

Structural Characterization. The microstructures of $Ge_{0.87}Pb_{0.13}Te$ and $Ge_{0.87}Pb_{0.13}Te$ + 3 mol % Bi_2Te_3 were fully characterized by transmission electron microscopy (TEM). Typically, two features are frequently observed in $Ge_{0.87}Pb_{0.13}Te$: irregular precipitates with sizes larger than 100 nm distributed in the uniformly contrasting matrix (Figure 3a) and regular lamellar structures free of precipitates (Figure 3b). The composition of the precipitates and the surrounding matrix were qualitatively determined by energy-dispersive spectroscopy (EDS), as shown in Figure 3c,d. Our results show that the precipitates are PbTe-rich while the matrix is GeTe-rich. This

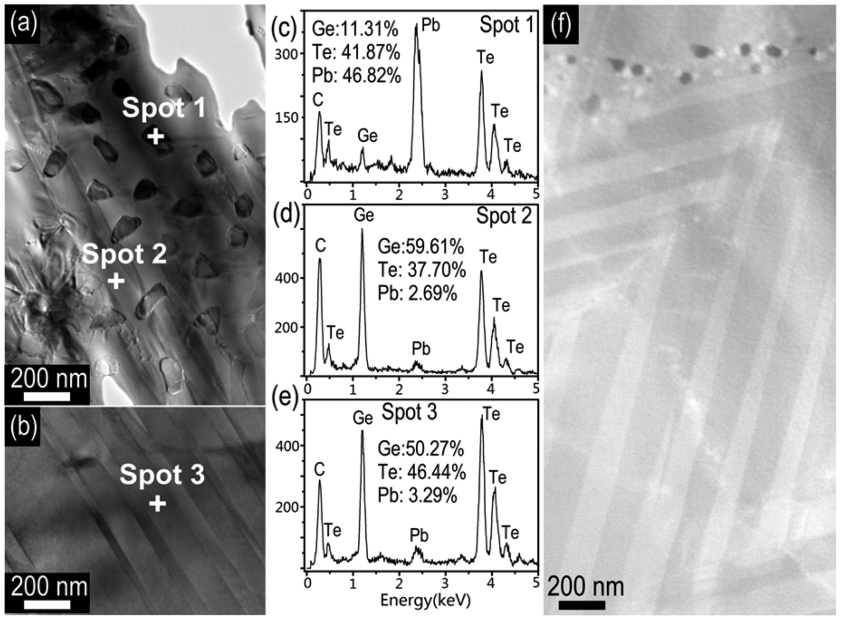

Figure 3. (a, b) Bright-field (BF) TEM images of (a) $Ge_{0.87}Pb_{0.13}Te$ with dense precipitates and (b) the domain variant areas free of precipitates. (c–e) EDS spectra of (c) the precipitate (spot 1) and (d) the matrix (spot 2) in (a) and (e) spot 3 in (b). (f) BF scanning TEM image of $Ge_{0.87}Pb_{0.13}Te$ + 3 mol % Bi_2Te_3 with domain structures and smaller precipitates.

dx.doi.org/10.1021/ja504896a | J. Am. Chem. Soc. 2014, 136, 11412–11419

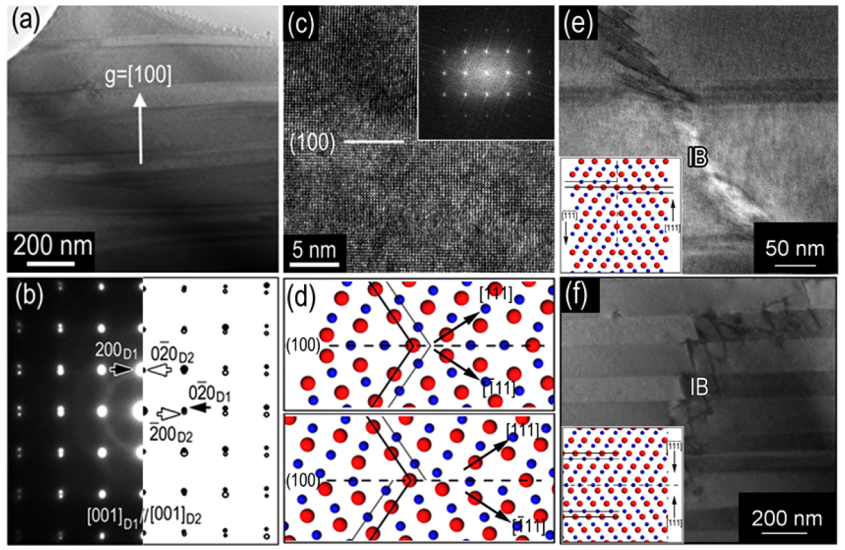

Figure 4. (100) twinning structures in $Ge_{0.87}Pb_{0.13}Te$. (a) BF TEM image and (b) corresponding experimental (left) and simulated (right) SAED patterns. (c) HRTEM image and (inset) fast Fourier transform. (d) Two possible atomic models of the (100) twin boundaries. (e, f) Inversion boundaries in (e) $Ge_{0.87}Pb_{0.13}Te$ and (f) $Ge_{0.87}Pb_{0.13}Te$ + 3 mol % Bi_2Te_3; atomic models of the two inversion boundaries are shown in the insets.

precipitation depletes the matrix of Pb, creating Ge-rich zones in the surroundings.[22] In the lamellar area shown in Figure 3b, a contrast difference is observed, and EDS analysis implies that this area is GeTe-rich (Figure 3e). In comparison, upon addition of Bi_2Te_3, fewer Pb-rich precipitates with much smaller grain sizes of ~50 nm are observed (Figure 3f). Apparently, the introduction of Bi_2Te_3 increases the solubility of PbTe in GeTe, which is also indicated by the aforementioned XRD patterns. The higher solubility of PbTe in the GeTe matrix upon Bi_2Te_3 doping creates more point defects and smaller nanostructures, both of which can impede the transport of charge carriers and acoustic phonons. This explains the strong reduction of the hole mobility and lattice thermal conductivity in $Ge_{0.87}Pb_{0.13}Te$ + 3 mol % Bi_2Te_3 compared with its Bi_2Te_3-free analogue.

Generally, the contrast difference observed in the lamellar area arises from the breakdown of Friedel symmetry for noncentrosymmetric crystals (i.e., domain variants).[28] As mentioned above, GeTe undergoes a transition at ~700 K from a high-temperature cubic phase to a low-temperature rhombohedral phase, and the evolution of the unit cell is schematically shown in Figure 1c. The crystal symmetry changes from $Fm\bar{3}m$ to $R3m$ and loses some point-symmetry operations but retains all of the translation operations. Theoretically, the possible orientation variants and domain boundaries formed during this displacive transition can be well-understood within the frame of group theory.[29] The detailed derivation is provided in the Supporting Information. Eight domain variants (D1−D8) are expected, and the crystallographic relationships therein are determined. The interfaces between different domain variants can be divided into two different types: twin boundaries ($m\langle 100\rangle$ and $m\langle 110\rangle$) and inversion boundaries ($\bar{1}$). Experimentally, the geometries of these twins can be identified from the contrast effects and diffraction patterns with the assistance of TEM.[30] At room temperature, as shown in Figure 4a, typical lamellar domains with darker and brighter contrast are present in the $Ge_{0.87}Pb_{0.13}Te$ sample. The corresponding selected-area electron diffraction (SAED) pattern in Figure 4b (left), which can be indexed as (100) twins of two variants D1 and D2, shows split spots along the ⟨100⟩ direction. The simulated SAED pattern is shown in Figure 4b (right) along with the detailed indices. The high-resolution TEM (HRTEM) lattice image in Figure 4c further proves the existence of the (100) twin boundary. Two possible atomic configurations are illustrated in Figure 4d. The (110)-type twinning in the $Ge_{0.87}Pb_{0.13}Te$ sample and the (100)- and (110)-type twinning structures in $Ge_{0.87}Pb_{0.13}Te$ + 3 mol % Bi_2Te_3 were also identified from the SAED patterns and are summarized in Figures S4 and S5 in the Supporting Information.

The inversion boundaries (IBs) can be determined from the specific contrast effects. The IBs in $Ge_{0.87}Pb_{0.13}Te$ and $Ge_{0.87}Pb_{0.13}Te$ + 3 mol % Bi_2Te_3 are shown in Figure 4e,f respectively, and typical α fringes due to the existence of inversion boundaries are observed.[28,30] The two possible atomic structures are shown in the insets in Figure 4e,f.

As discussed above, regions with uniform contrast are also frequently imaged in these two samples. In principle, the formation of the twin-related domains arises from the strain energy relaxation[31,32] and results in the contrast difference between different domains. In the Ge-rich matrix, however, GeTe exists in the form of monodomain grains, as evidenced by the SAED pattern presented in Figure S6b in the Supporting Information, while the GeTe polydomains with distinguished contrasts in a large grain are shown in Figure S6d.

We can conclude that the PbTe−GeTe interface plays a role in relaxing the strain energy in the isolated GeTe monodomain grains. In the polydomain grains, the domain boundaries act as the strain relaxation sources. Moreover, above the phase transition temperature, the aforementioned domain boundaries tend to disappear during the phase transition process. Along with the disappearance of the twin structures, we observed neither an increase in the lattice thermal conductivity nor an enhancement of the electrical conductivity, indicating the fairly weak role of these twin boundaries in scattering of acoustic phonons and charge carriers. This is normally expected for coherent boundaries,[33] which were proved to be ineffective in scattering charge carriers and phonons. In contrast, the point defects and PbTe precipitate boundaries are believed to reduce the lattice thermal conductivity in $Ge_{0.87}Pb_{0.13}Te$ even at high temperatures. In $Ge_{0.87}Pb_{0.13}Te$ + 3 mol % Bi_2Te_3, additional Pb and Bi point defects strongly enhance the phonon scattering

dx.doi.org/10.1021/ja504896a | J. Am. Chem. Soc. 2014, 136, 11412−11419

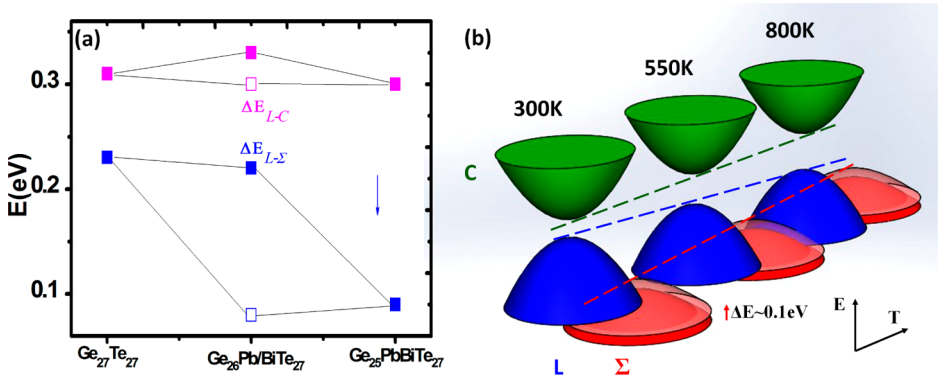

Figure 5. (a) DFT calculations showing that doping with Bi_2Te_3 (open squares) can reduce the energy offsets between the L and Σ valence bands more significantly compared with PbTe alloying (solid squares). (b) Schematic illustration of the band offsets among the L, Σ, and C bands. As the temperature increases, the energy offset between the L and Σ valence bands decreases while that between the L and C bands increases. Upon the dissolution of Bi_2Te_3, thereby promoting the solubility of PbTe in GeTe, the Σ valence band is lifted up by ∼0.1 eV, indicating a greater involvement of the Σ band in electrical transport.

and further reduce the overall lattice thermal conductivity, as shown in Figure 2e.

Band Structure Discussions. PbTe has been meticulously studied over decades,[3,26,34] and its impressive thermoelectric properties mainly stem from the low thermal conductivity and outstanding thermopower. The former can be achieved via various hierarchical nanoengineering techniques.[4] The large thermopower is attributed to the high band degeneracy, especially in p-type PbTe, where the lower heavy Σ valence band at ⟨110⟩ with a degeneracy of 12 could contribute significantly to electrical conduction in addition to the upper light L valence band at ⟨111⟩ with a degeneracy of 4.[3,26,35] The effective convergence of these two valence bands in p-type PbTe at medium and high temperatures or at high carrier concentrations can greatly enhance the charge carriers' effective mass, assuring a high thermopower without sacrificing electrical conductivity.

Similar to PbTe, it was suggested[8,10,36] that the band structure of the high-temperature cubic phase of GeTe resembles that of PbTe, with four ⟨111⟩ extrema around the L point and 12 ⟨110⟩ extrema around Σ in k space. When GeTe experiences a cubic-to-rhombohedral ferroelectric phase transition around 700 K, the previous $Fm\bar{3}m$ symmetry is then lowered to $R3m$; correspondingly, the initial fourfold-degenerate light L band splits into one valley with C_{3v} symmetry along the direction of the relative sublattice displacement and three other equivalent ones with C_s symmetry. Meanwhile, the heavy Σ band splits into sixfold $[110][101][011][\bar{1}10][\bar{1}0\bar{1}][0\bar{1}\bar{1}]$ valleys and sixfold $[1\bar{1}0][10\bar{1}][01\bar{1}][\bar{1}10][\bar{1}01][0\bar{1}1]$ ones, as discussed by Plachkova and Georgiev[36] and Christakudi et al.[8] However, since the face-centered rhombohedral (fcr) phase is nearly cubic, the splitting of initially degenerate bands is of a negligible magnitude, and it was thus assumed by Tsu et al.[11] that to a first-order approximation the band structure of GeTe may be treated in terms of the cubic phase over the entire temperature range. With this cubic phase assumption, they conducted calculations based on a four-band model (two valence bands + two conduction bands) and obtained good agreement with the experimental values. The rationale for this model and corresponding band parameters determined by experimental fitting was previously justified by Shubnikov–de Haas measurements[37] on the SnTe system. This first-order approximation was adopted in this work and was found to be fairly proper for the purpose of explaining the observed thermoelectric properties.

The evidence[10,38] indicates that the second valence band (Σ band) in GeTe must be well-separated in energy from the L band, and the energetic difference between the L and Σ bands ($\Delta E_{L-\Sigma}$) is about 0.27–0.38 eV[9,10,39] at 300 K, although it might vary with the doping level. It is interesting to see how $\Delta E_{L-\Sigma}$ is affected by alloying of Pb in the GeTe matrix and Bi_2Te_3 doping in the GeTe matrix.

DFT electronic structure calculations on NaCl-type GeTe with various dopants/alloying elements were performed in order to gain insights into the effects of dopants on the band levels. As shown in Figure 5a, the introduction of 3.7 mol % PbTe into GeTe increases the energy offset between the L and C bands (ΔE_{L-C}) by ∼0.02 eV and decreases $\Delta E_{L-\Sigma}$ by ∼0.01 eV. In comparison, doping with the same amount of Bi_2Te_3 lifts the Σ band up and significantly reduces $\Delta E_{L-\Sigma}$ by ∼0.14 eV, compared with ∼0.01 eV due to PbTe alloying. Such a reduction suggests a much greater contribution to charge transport from the heavy Σ valence band, as will be discussed later. Nevertheless, it should be noted that we still cannot exclude the possibility that the dissolution of nearly 13 mol % PbTe (up from 3.7 mol %) into GeTe due to Bi_2Te_3 doping is also responsible for the reduced band offsets $\Delta E_{L-\Sigma}$.

The band gap ΔE_{L-C} in GeTe at 300 K was estimated to be 0.2–0.23 eV,[10,11,40] while $\Delta E_{L-\Sigma}$ is around 0.27–0.38 eV.[9,10,39] As for their temperature dependences, an overall increasing trend for ΔE_{L-C} was reported by Lewis[10] and Korzhuev,[39] while that of $\Delta E_{L-\Sigma}$ was still unclear. In the present work, within the cubic phase assumption, ΔE_{L-C} was assumed to increase linearly while $\Delta E_{L-\Sigma}$ was presumed to decrease continuously with temperature, as reported for its analogue PbTe.[3,26] The rates of change of $\Delta E_{L-\Sigma}$ and ΔE_{L-C} with temperature were adjusted to give the best agreement with experiments (see the Supporting Information) and are schematically presented in Figure 5b.

Three-Band Model Calculations on the Charge Transport Properties. To better understand the origin of these outstanding thermoelectric properties, especially that of the thermopower for $Ge_{0.87}Pb_{0.13}Te$ doped with 3 mol % Bi_2Te_3, we present theoretical simulations of the transport properties of these three GeTe compositions over the temperature range from 300 to 800 K within the framework of a three-band model (L + Σ + C) based on the Boltzmann transport equation (BTE)

dx.doi.org/10.1021/ja504896a | J. Am. Chem. Soc. 2014, 136, 11412–11419

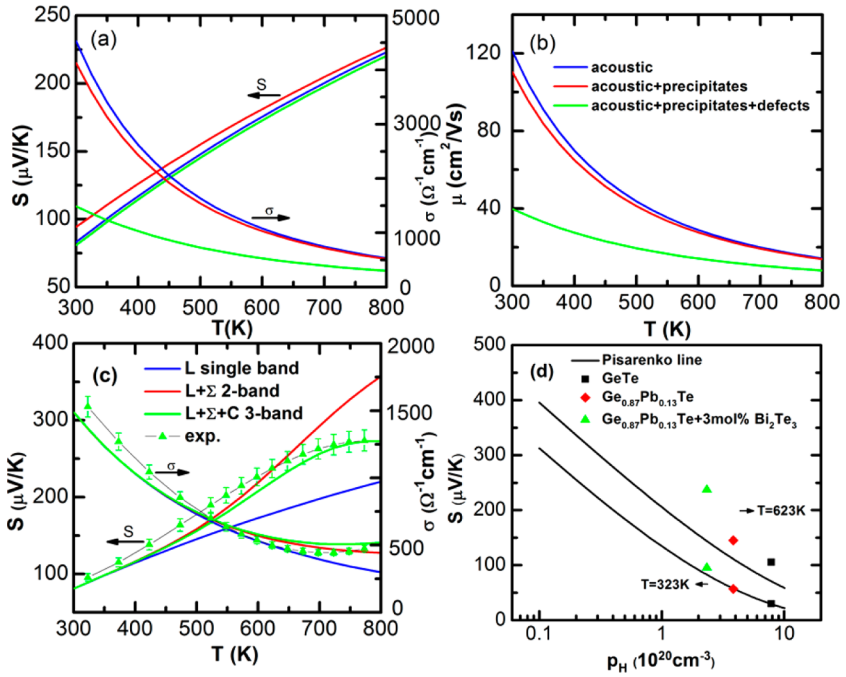

Figure 6. (a, b) Simulated results showing the different effects of incorporating precipitate and point-defect scattering in the framework of a single L band on (a) the thermopower S and electrical conductivity σ and (b) the carrier mobility μ in $Pb_{0.13}Ge_{0.87}Te$ + 3 mol % Bi_2Te_3. (c) Simulated thermopower S and electrical conductivity σ involving a single-band (L) model (blue), a two-band (L + Σ) model (red), and a three-band (L + Σ + C) model (green), shown separately for comparison with experimental values of $Ge_{0.87}Pb_{0.13}Te$ + 3 mol % Bi_2Te_3. (d) Pisarenko lines compared with plots of the experimental thermopower S versus hole carrier concentration (p_H) at 323 and 623 K, indicating an enhancement of the thermopower and suggesting the contribution of a second valence band in the charge transport process at elevated temperatures.

and an energy-dependent relaxation time approximation within the Kane band assumption (eq S9 in the Supporting Information). Apart from acoustic phonon scattering, we also incorporate other mechanisms, including point-defect and precipitate scattering, as will be seen below.

Before we deal with the three-band model, we shall discuss the electrical conduction in a single-band model in order to introduce point defects and precipitate scattering. Specific expressions for the single-band model are presented in the Supporting Information (eqs S10−S13). In the case of pristine GeTe, the dominant scattering is assumed to be acoustic phonon scattering[3,35,41] with a relaxation time τ_{ac}. However, in the presence of point defects arising from doping or alloying (with a relaxation time τ_d) and of nanoscale precipitates originating from phase separation or immiscibility (with a relaxation time τ_i), as in the cases of $Ge_{0.87}Pb_{0.13}Te$ and $Ge_{0.87}Pb_{0.13}Te$ + 3 mol % Bi_2Te_3, the overall relaxation time can be written as a combination of the relaxation times for these three individual scattering mechanisms, expressed following the Matthiessen's rule as:

$$\frac{1}{\tau} = \frac{1}{\tau_{ac}} + \frac{1}{\tau_d} + \frac{1}{\tau_i} \quad (1)$$

Detailed expressions for the relaxation times τ_{ac}, τ_d, and τ_i can be found in the Supporting Information (eqs S14−S16). It was reported[8] that the solubility of Bi_2Te_3 in GeTe is around 5%, and thus, all of the Bi_2Te_3 used in our sample should be dissolved in the GeTe matrix as point defects, consistent with our TEM and XRD observations. For PbTe, since nanoscale Pb-rich precipitates (50−100 nm) were seen in both $Ge_{0.87}Pb_{0.13}Te$ and $Ge_{0.87}Pb_{0.13}Te$ + 3 mol % Bi_2Te_3 (with a larger number density in $Ge_{0.87}Pb_{0.13}Te$ than in $Ge_{0.87}Pb_{0.13}Te$ + 3 mol % Bi_2Te_3), as shown in Figure 3, it can be concluded that a portion of the PbTe precipitated as a nanophase while the remaining fraction dissolved in the GeTe matrix, creating point defects.

To uncover the distinct roles of precipitates and point defects in the charge carrier scattering process, calculations of σ and S in $Ge_{0.87}Pb_{0.13}Te$ + 3 mol % Bi_2Te_3 are discussed in the framework of a single nonparabolic Kane band model. Upon the precipitation of nanoscale Pb-rich phases, their interfaces/boundaries with the main GeTe-based matrix might impede charge carrier transport via the so-called energy filtering effect.[42] Specifically, the flow of low-energy (E less than the interface potential V_0) holes can be effectively impeded while the transport of high-energy ($E > V_0$) holes remains uninterrupted. Besides reducing the electrical conductivity σ via enhanced boundary scattering, the preferential filtering of low-energy charge carriers can also effectively reduce the negative contribution from low-energy charge carriers to the thermopower and thus lead to a net enhancement in S, as discussed elsewhere.[42,43]

Compared with the precipitate scattering, point defects play a much more obvious role in impeding charge carrier transport. This is the case because point defects are atomic-scale defects, which are much closer to the characteristic wavelength of charge carriers than are nanoscale (50−100 nm) precipitates. Point defects therefore primarily account for the reduced electrical conductivity σ, as depicted in Figure 6a. It is noteworthy that the relative effects of both precipitates and point defects on charge carrier scattering are weakened with rising temperature, and the transport properties (S and σ) calculated considering all three scattering mechanisms gradually approach those incorporating acoustic phonon scattering only (Figure 6a). This can be explained by the much stronger

dx.doi.org/10.1021/ja504896a | J. Am. Chem. Soc. 2014, 136, 11412−11419

dependence of acoustic phonon scattering on temperature compared with point-defect and precipitate scattering, as expressed in eqs S14−S16 in the Supporting Information. As the temperature increases, the relaxation time of acoustic phonon scattering τ_{ac} decreases much faster than τ_d and τ_i and tends to dominate the scattering process. It also follows from Figure 6b that the carrier mobility significantly decreases upon the involvement of precipitates and point defects, further supporting the above discussions.

In a single parabolic band model, in the case of strong degeneracy the thermopower S increases linearly with temperature (provided that the carrier concentration n and effective mass m^* are kept constant[44]) according to

$$S = \frac{8\pi^2 {k_B}^2}{3eh^2} m_d^* T \left(\frac{\pi}{3n}\right)^{2/3} \quad (2)$$

Even in the case of a nonparabolic Kane model, the dependence of the thermopower on temperature deviates little from the linear trend. Clearly, in this single nonparabolic L band model, the calculated thermopower for the composition $Ge_{0.87}Pb_{0.13}Te$ + 3 mol % Bi_2Te_3 differs from the experimental results, especially at elevated temperatures, as indicated by the blue solid line (single band model) and green triangles in Figure 6c. Only by incorporating the contribution from the heavy Σ valence band could the thermopower S exhibit a steeply increasing climb with temperature (red solid line, two-band model) resembling the experimental trend until being ultimately suppressed by the bipolar diffusion (green solid line, three-band model) at even higher temperatures.

The necessity of introducing the second valence band is also suggested by comparing Pisarenko plots[27] with the experimental Seebeck values (Figure 6d). The effective mass m^* used to plot the Pisarenko lines is $1.3m_0$, which belongs to the single L band. At 323 K, the experimental thermopower values fall close to the Pisarenko line. However, as the temperature climbs to 623 K, the thermopower values of all three compositions ascend clearly above the corresponding Pisarenko line. The enhanced thermopower can be explained only by the incorporation of the second valence band with a much heavier effective hole mass. It is also remarkable that among all three compositions the thermopower of $Ge_{0.87}Pb_{0.13}Te$ + 3 mol % Bi_2Te_3 deviates the most above the Pisarenko lines, considering that this composition has the lowest hole carrier concentration (p_H), the stronger contribution of the second valence band can only come from the narrower energy separation between L and Σ valence bands. This conclusion is consistent with our aforementioned DFT calculations.

In the L + Σ + C three-band model, the overall electrical conductivity σ and thermopower S derive from the individual contributions from the two valence bands (L, Σ) and the conduction band (C) as follows:[3,26]

$$\sigma = \sigma_L + \sigma_\Sigma + \sigma_C \quad (3)$$

$$S = \frac{\sigma_L S_L + \sigma_\Sigma S_\Sigma - \sigma_C S_C}{\sigma_L + \sigma_\Sigma + \sigma_C} \quad (4)$$

Compared with the two-band model (L + Σ), the incorporation of the C band results in a saturated thermopower S and a slightly higher electrical conductivity σ at elevated temperatures.

The bipolar effect was explicitly included in the modeling by taking the conduction band together with the two valence bands into consideration for the electronic transport calculations. The thermoelectric performance would have been much better without the presence of bipolar diffusion, as indicated by the contrast between the red solid line for the L + Σ two-band model and the green solid line for the three-band model (Figure 6c). It is interesting to observe that the effect of bipolar diffusion on the thermopower becomes much more obvious as the hole carrier concentration decreases from PbTe ($p_H \approx 7.85 \times 10^{20}$ cm^{-3}) to $Ge_{0.87}Pb_{0.13}Te$ ($p_H \approx 3.85 \times 10^{20}$ cm^{-3}) and to $Ge_{0.87}Pb_{0.13}Te$ + 3 mol % Bi_2Te_3 ($p_H \approx 2.34 \times 10^{20}$ cm^{-3}) (Figure 2a). This phenomenon suggests that the Fermi level (E_F) moves closer to the conduction band with the addition of PbTe and Bi_2Te_3. The relative position of E_F is determined by the effective mass m^* (determined by local band structure) and the carrier concentration n, as shown in eq S10 in the Supporting Information. Considering the similar local band structures/E−k relations for all three compositions, E_F is then determined largely by the carrier concentration. In p-type semiconductors, when the carrier concentration decreases, E_F moves toward the conduction band. The closer E_F is to the conduction band, the larger is the probability that electrons are thermally excited into the conduction band, and therefore, the bipolar diffusion ought to be most obvious in the material with the lowest hole concentration, namely, $Ge_{0.87}Pb_{0.13}Te$ + 3 mol % Bi_2Te_3. Similar trends were also observed in heavily doped PbTe.[45]

Overall, our calculations based on the three-band model show good agreement with the experimental thermoelectric transport properties of GeTe, $Ge_{0.87}Pb_{0.13}Te$, and $Ge_{0.87}Pb_{0.13}Te$ + 3 mol % Bi_2Te_3. They not only justify our use of the cubic phase assumption but also suggest that involvement of the heavy valence band (Σ) is crucial in achieving a significant enhancement of the thermopower. On the basis of the DFT calculations as well as our simulations in the framework of the three-band model, we believe that the introduction of Bi_2Te_3 into $Ge_{0.87}Pb_{0.13}Te$ pushes the two valence bands (L and Σ) closer in energy, enabling the heavy valence band to contribute notably to the electrical conduction via thermal excitation of holes from the L band to the Σ band. The mechanism is similar to those found in lead chalcogenides, such as the PbTe−PbS,[46] PbTe−MnTe,[47] PbTe−MgTe,[48] PbSe−SrSe,[4c] and PbSe−CdS[49] systems.

■ CONCLUSIONS

Extraordinary thermoelectric performance is obtained in GeTe when it is simultaneously alloyed with PbTe and doped with Bi_2Te_3, leading to a ZT value of ∼1.9. While alloying PbTe into GeTe creates nanostructuring, our studies reveal that the high performance in this system is largely due to Bi_2Te_3 doping, which has three main significant effects: (a) it reduces the carrier concentration, thereby enhancing the thermopower; (b) it brings the two valence bands (L and Σ) closer in energy (smaller $\Delta E_{L-\Sigma}$), thus facilitating a greater contribution from the Σ band, which further increases the thermopower; (c) it sharply increases the number of point defects, leading to a significant reduction in the lattice thermal conductivity. Moreover, doping with Bi_2Te_3 controls the solubility of PbTe in the GeTe matrix. This has a profound effect on the lattice thermal conductivity and the level of Ge vacancies, which also contributes to the high thermoelectric performance. Our work also shows that not all boundaries affect the transport properties equally. For example, boundaries between twin structures in the GeTe rhombohedral phase appear to be of

negligible importance in scattering charge carriers and phonons. These findings create new insights that pave the way for further improvements in the thermoelectric performance of GeTe-based as well as other types of thermoelectric materials.

■ ASSOCIATED CONTENT

Supporting Information

Experimental procedures and calculation methods, group theory analysis, and the three-band model incorporating precipitate and point-defect scattering. This material is available free of charge via the Internet at http://pubs.acs.org.

■ AUTHOR INFORMATION

Corresponding Authors

he.jq@sustc.edu.cn
m-kanatzidis@northwestern.edu

Author Contributions

#D.W. and L.-D.Z. contributed equally.

Notes

The authors declare no competing financial interest.

■ ACKNOWLEDGMENTS

This contribution was supported by startup funds from South University of Science and Technology of China and also as part of the Center for Revolutionary Materials for Solid State Energy Conversion, an Energy Frontier Research Center funded by the U.S. Department of Energy, Office of Science, Office of Basic Energy Sciences, under Award DE-SC0001054. In addition, the authors acknowledge the United States−Israel Binational Science Foundation (BSF), Grant 2008114, for partial support of this research. The authors also thank Xuetao Shen for help with the TEM studies.

■ REFERENCES

(1) Heremans, J. P.; Jovovic, V.; Toberer, E. S.; Saramat, A.; Kurosaki, K.; Charoenphakdee, A.; Yamanaka, S.; Snyder, G. J. *Science* **2008**, *321*, 554.

(2) Liu, W.; Tan, X.; Yin, K.; Liu, H.; Tang, X.; Shi, J.; Zhang, Q.; Uher, C. *Phys. Rev. Lett.* **2012**, *108*, 166601.

(3) Pei, Y.; Shi, X.; LaLonde, A.; Wang, H.; Chen, L.; Snyder, G. J. *Nature* **2011**, *473*, 66.

(4) (a) Biswas, K.; He, J.; Blum, I. D.; Wu, C. I.; Hogan, T. P.; Seidman, D. N.; Dravid, V. P.; Kanatzidis, M. G. *Nature* **2012**, *489*, 414. (b) Wu, H. J.; Zhao, L. D.; Zheng, F. S.; Wu, D.; Pei, Y. L.; Tong, X.; Kanatzidis, M. G.; He, J. Q. *Nat. Commun.* **2014**, *5*, 4515. (c) Zhao, L. D.; Dravid, V. P.; Kanatzidis, M. G. *Energy Environ. Sci.* **2014**, *7*, 251. (d) Wu, H. J.; Carrete, J.; Zhang, Z.; Qu, Y.; Shen, X.; Wang, Z.; Zhao, L.-D.; He, J. *NPG Asia Mater.* **2014**, *6*, e108.

(5) Zhao, L.-D.; Lo, S.-H.; Zhang, Y.; Sun, H.; Tan, G.; Uher, C.; Wolverton, C.; Dravid, V. P.; Kanatzidis, M. G. *Nature* **2014**, *508*, 373.

(6) Bhattacharya, S.; Pope, A.; Littleton, R., IV; Tritt, T. M.; Ponnambalam, V.; Xia, Y.; Poon, S. *Appl. Phys. Lett.* **2000**, *77*, 2476.

(7) Pei, Y.; Lensch-Falk, J.; Toberer, E. S.; Medlin, D. L.; Snyder, G. J. *Adv. Funct. Mater.* **2011**, *21*, 241.

(8) Christakudi, T. A.; Plachkova, S. K.; Christakudis, G. C. *Phys. Status Solidi A* **1995**, *147*, 211.

(9) Lewis, J. E. *Phys. Status Solidi B* **1970**, *38*, 131.

(10) Lewis, J. E. *Phys. Status Solidi B* **1973**, *59*, 367.

(11) Tsu, R.; Howard, W. E.; Esaki, L. *Phys. Rev.* **1968**, *172*, 779.

(12) Mazelsky, R.; Lubell, M. S. In *Nonstoichiometric Compounds*; Advances in Chemistry, Vol. *39*; American Chemical Society: Washington, DC, 1963; pp 210−217.

(13) Damon, D. H.; Lubell, M. S.; Mazelsky, R. *J. Phys. Chem. Solids* **1967**, *28*, 520.

(14) Cook, B.; Wei, X.; Harringa, J.; Kramer, M. *J. Mater. Sci.* **2007**, *42*, 7643.

(15) Polking, M. J.; Han, M.-G.; Yourdkhani, A.; Petkov, V.; Kisielowski, C. F.; Volkov, V. V.; Zhu, Y.; Caruntu, G.; Alivisatos, A. P.; Ramesh, R. *Nat. Mater.* **2012**, *11*, 700.

(16) Avramova, I. A.; Plachkova, S. K. *J. Phys.: Condens. Matter* **2001**, *13*, 43.

(17) Plachkova, S. K.; Tersiev, L. A. *Phys. Status Solidi B* **1984**, *125*, 659.

(18) Thompson, A. J.; Sharp, J. W.; Rawn, C. J. *J. Elec. Mater.* **2009**, *38*, 1407.

(19) Konstantinov, P. P.; Shelimova, L. E.; Avilov, E. S.; Kretova, M. A.; Zemskov, V. S. *Inorg. Mater.* **2001**, *37*, 662.

(20) Gelbstein, Y.; Dado, B.; Ben-Yehuda, O.; Sadia, Y.; Dashevsky, Z.; Dariel, M. *J. Elec. Mater.* **2010**, *39*, 2049.

(21) Gelbstein, Y.; Dashevsky, Z.; Dariel, M. P. *Physica Status Solidi RRL* **2007**, *1*, 232.

(22) Gelbstein, Y.; Davidow, J.; Girard, S. N.; Chung, D. Y.; Kanatzidis, M. *Adv. Energy Mater.* **2013**, *3*, 815.

(23) Volykhov, A. A.; Yashina, L. V.; Shtanov, V. I. *Inorg. Mater.* **2006**, *42*, 596.

(24) Mazelsky, R.; Lubell, M. S.; Kramer, W. E. *J. Chem. Phys.* **1962**, *37*, 45.

(25) Lubell, M. S.; Mazelsky, R. *J. Electrochem. Soc.* **1963**, *110*, 520.

(26) Ravich, Y. I. *Semiconducting Lead Chalcogenides*; Plenum: New York, 1970.

(27) Zhao, L. D.; Lo, S. H.; He, J.; Li, H.; Biswas, K.; Androulakis, J.; Wu, C. I.; Hogan, T. P.; Chung, D. Y.; Dravid, V. P.; Kanatzidis, M. G. *J. Am. Chem. Soc.* **2011**, *133*, 20476.

(28) Gevers, R.; Delavignette, P.; Blank, H.; Van Landuyt, J.; Amelinckx, S. *Phys. Status Solidi B* **1964**, *5*, 595.

(29) Guymont, M. *Phys. Rev. B* **1978**, *18*, 5385.

(30) Snykers, M.; Delavignette, P.; Amelinckx, S. *Mater. Res. Bull.* **1972**, *7*, 831.

(31) Polking, M. J.; Zheng, H.; Ramesh, R.; Alivisatos, A. P. *J. Am. Chem. Soc.* **2011**, *133*, 2044.

(32) Pompe, W.; Gong, X.; Suo, Z.; Speck, J. S. *J. Appl. Phys.* **1993**, *74*, 6012.

(33) He, J.; Kanatzidis, M. G.; Dravid, V. P. *Mater. Today* **2013**, *16*, 166.

(34) Smirnov, I. A.; Vinogradova, M. N.; Kolomoets, N. V.; Sysoeva, L. M. *Sov. Phys. Solid State, Ussr* **1968**, *9*, 2074.

(35) Pei, Y.; Wang, H.; Snyder, G. J. *Adv. Mater.* **2012**, *24*, 6125.

(36) Plachkova, S. K.; Georgiev, T. I. *Phys. Status Solidi A* **1993**, *136*, 509.

(37) Burke, J.; Allgaier, R.; Houston, B.; Babiskin, J.; Siebenmann, P. *Phys. Rev. Lett.* **1965**, *14*, 360.

(38) Bahl, S. K.; Chopra, K. L. *J. Appl. Phys.* **1970**, *41*, 2196.

(39) Korzhuev, M. A. *Phys. Status Solidi B* **1982**, *112*, 39.

(40) Tung, Y.; Cohen, M. *Phys. Rev.* **1969**, *180*, 823.

(41) Faleev, S. V.; Léonard, F. *Phys. Rev. B* **2008**, *77*, 214304.

(42) Moyzhes, B.; Nemchinsky, V. *Appl. Phys. Lett.* **1998**, *73*, 1895.

(43) Zeng, G.; Zide, J. M. O.; Kim, W.; Bowers, J. E.; Gossard, A. C.; Bian, Z.; Zhang, Y.; Shakouri, A.; Singer, S. L.; Majumdar, A. *J. Appl. Phys.* **2007**, *101*, 034502.

(44) Snyder, G. J.; Toberer, E. S. *Nat. Mater.* **2008**, *7*, 105.

(45) Pei, Y.; LaLonde, A.; Iwanaga, S.; Snyder, G. J. *Energy Environ. Sci.* **2011**, *4*, 2085.

(46) Girard, S. N.; He, J.; Zhou, X.; Shoemaker, D.; Jaworski, C. M.; Uher, C.; Dravid, V. P.; Heremans, J. P.; Kanatzidis, M. G. *J. Am. Chem. Soc.* **2011**, *133*, 16588.

(47) Pei, Y.; Wang, H.; Gibbs, Z. M.; LaLonde, A. D.; Snyder, G. J. *NPG Asia Mater.* **2012**, *4*, e28.

(48) Zhao, L. D.; Wu, H. J.; Hao, S. Q.; Wu, C. I.; Zhou, X. Y.; Biswas, K.; He, J. Q.; Hogan, T. P.; Uher, C.; Wolverton, C.; Dravid, V. P.; Kanatzidis, M. G. *Energy Environ. Sci.* **2013**, *6*, 3346.

(49) Zhao, L. D.; Hao, S.; Lo, S. H.; Wu, C. I.; Zhou, X.; Lee, Y.; Li, H.; Biswas, K.; Hogan, T. P.; Uher, C.; Wolverton, C.; Dravid, V. P.; Kanatzidis, M. G. *J. Am. Chem. Soc.* **2013**, *135*, 7364.